ACS APPLIED ELECTRONIC MATERIALS

pubs.acs.org/acsaelm

Article

Improving Light Stability of Nonfullerene Acceptor Inverted Organic Solar Cell by Incorporating a Mixed Nanocomposite Metal Oxide Electron Transporting Layer

Apostolos Ioakeimidis,* Fedros Galatopoulos, Alina Hauser, Michael Rossier, and Stelios A. Choulis*

Cite This: ACS Appl. Electron. Mater. 2025, 7, 3940−3946

Read Online

ACCESS | Metrics & More | Article Recommendations | Supporting Information

ABSTRACT: We present significant light stability enhancement of nonfullerene acceptor inverted organic photovoltaics by incorporating a mixed nanocomposite metal oxide electron transporting layer. Using an appropriate mixture of ZnO:SnO_2 nanoparticles as an electron transporting layer in a PBDB-TF-T1 (T1):IT4F based organic solar cell device mitigates light induced photodegradation by lowering the defect formation at the active layer interface. We propose that the mixed metal oxide ETL act as hole scavengers that reduces the photocatalytic reaction of its surface. The optimized nanocomposite mixture of ZnO:SnO_2 10:90 (%V) provides higher light stability (ISOS-L2 protocol), prolonging the inverted OSCs lifetime (80% of the initial PCE, T80) by ∼16.5 times compared to the commonly used pristine ZnO electron transporting layer.

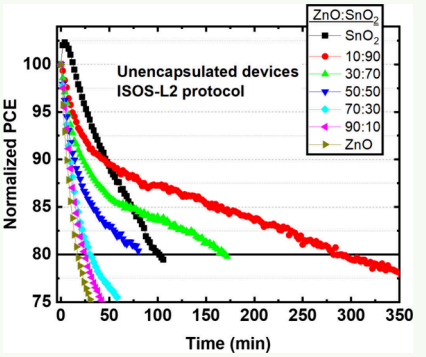

KEYWORDS: *organic photovoltaics, metal oxides, electron transporting layers, lifetime, inverted organic solar cells*

INTRODUCTION

Organic solar cells (OSCs) constitute one of the most promising next-generation photovoltaic technologies for implementation in a vast number of applications. The intense research and development in terms of materials and devices have resulted in an increase of OSC power conversion efficiency (PCE), reaching the milestone of ∼20%.[1,2] While PCE is one prerequisite toward organic photovoltaics commercialization, additional challenges need to be addressed. The most impactful limitation is the long-term stability of OSC hindering their widespread adoption.[3] The various degradation mechanisms occur within the bulk of the device's functional layers as well as at their interfaces due to stressing factors including oxygen, moisture, high temperature, and UV content of light.[4−6] Implementation of sophisticated materials and processes have demonstrated the potential of extending the operating lifetime under controlled conditions to thousands of hours.[7−10] Nevertheless, additional factors that impact the commercialization of OPVs must be taken into consideration such as raw materials cost, synthesis and processing complexity, toxicity, etc.[11−14]

The material properties of common metal oxides such as the high optical band gap, stability, facile energy levels, and electrical tunability in combination with nature abundant raw materials, easy synthesis, and low-cost processing render them a strong candidate for charge transporting layers in commercial OPVs. Regarding the so-called inverted structure, which is the commercially preferred structure for large scale production, the commonly used electron transporting layers (ETLs) and hole transporting layers (HTLs) are ZnO and MoO_3, respectively. Beyond these common metal oxides, a variety of pristine and modified metal oxides have been successfully applied as ETLs and HTLs, resulting in improved PCE and lifetime.[15−19] Nevertheless, the proven photocatalytic reactivity of front contact metal oxides can have a detrimental effect on the stability of OSCs through degradation of the active layer. Passivation of metal oxide photocatalytic sites at the interface with the active layer is a common strategy to alleviate surface reactivity.[20−24] Jiang et al. demonstrated that an SnO_2 ETL has a reduced photocatalytic effect on the IT4F improving the light stability of OPV compared to ZnO.[25] Recently, Park et al. improved the photostability of a nonfullerene acceptor (NFA) OPV by replacing the common ZnO ETL with a UV-A-insensitive titanium suboxide layer that suppressed the photocatalytic effect.[26]

In this manuscript we demonstrate a facile and scalable strategy to improve the OSC light stability implementing a mixed nanocomposite metal oxide ZnO:SnO_2 ETL. We study a full scale ratio of ZnO:SnO_2 mixed metal oxide nanoparticles

Received: January 29, 2025
Revised: April 14, 2025
Accepted: April 14, 2025
Published: April 24, 2025

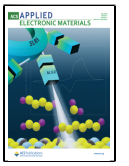

Table 1. Best PCE Devices under AM1.5 G Light Incorporating Various Ratios of Mixed ZnO:SnO_2 NP ETL with Their Corresponding V_{oc}, J_{sc}, and FF Parameters[a]

ZnO:SnO_2 (%V)	V_{oc} (V)	Jsc (mA/cm^2)	FF (%)	PCE (%)
0:100	0.94 (0.94 ± <0.005)	15.37 (15.39 ± 0.39)	57.21 (55.99 ± 0.82)	8.27 (8.10 ± 0.17)
10:90	0.94 (0.94 ± <0.005)	16.69 (16.19 ± 0.46)	59.00 (58.67 ± 0.47)	9.26 (8.94 ± 0.35)
30:70	0.94 (0.94 ± < 0.005)	16.86 (16.43 ± 0.37)	59.84 (59.91 ± 0.46)	9.49 (9.27 ± 0.23)
50:50	0.94 (0.94 ± <0.005)	16.71 (16.40 ± 0.34)	61.23 (61.00 ± 0.33)	9.62 (9.43 ± 0.16)
70:30	0.96 (0.96 ± <0.005)	17.07 (16.49 ± 0.47)	60.5 (61.31 ± 0.75)	9.92 (9.67 ± 0.33)
90:10	0.96 (0.96 ± <0.005)	17.17 (16.82 ± 0.24)	63.15 (63.15 ± 0.24)	10.41 (10.16 ± 0.15)
100:0	0.96 (0.96 ± <0.005)	17.85 (17.27 ± 0.67)	62.62 (61.95 ± 1.07)	10.73 (10.22 ± 0.50)

[a]The mean values and standard deviations obtained out of 16 different devices for each batch are given in parentheses.

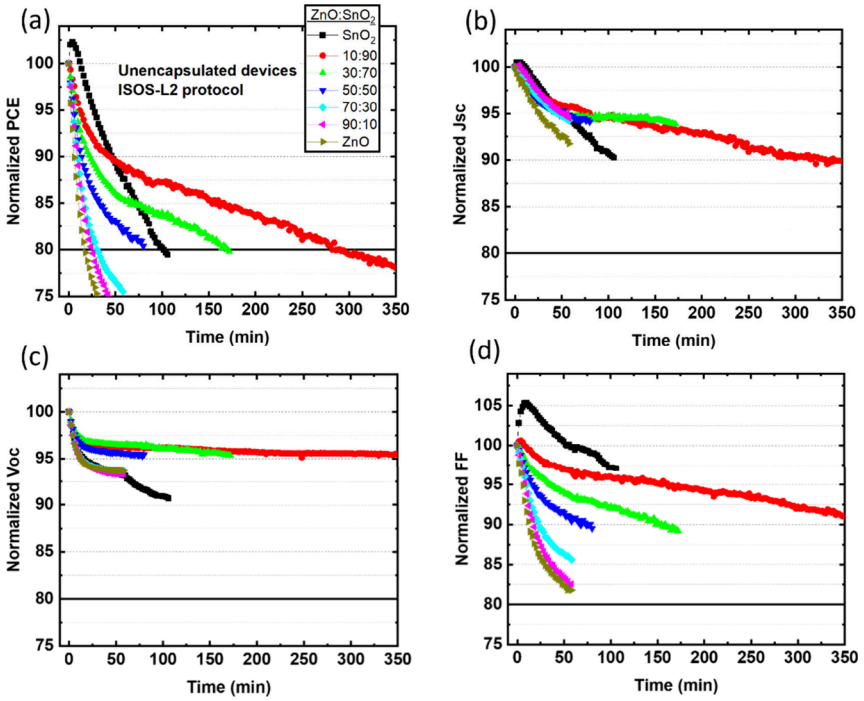

Figure 1. Normalized (a) PCE, (b) J_{sc}, (c) V_{oc}, and (d) FF of unencapsulated T1:IT4F based inverted OSC incorporating various ratios of mixed oxide ZnO:SnO_2 ETLs as a function of exposure time under the ISOS-L2 protocol.

(NPs) as ETLs using ITF4 as the active layer acceptor ,which is very sensitive to the photocatalytic effect of the ZnO layer.[25] The implementation of a 10:90 ratio ZnO:SnO_2 NP ETL in an inverted device structure results in ∼16.5 and ∼2.8 times improved light stability (ISOS-L2 protocol) compared to pristine ZnO and SnO_2, respectively. The produced energy until 80% of the initial power conversion efficiency (PCE) for the 10:90 ratio ZnO:SnO_2 is about ∼13.2 and ∼3.0 times higher compared to the corresponding ZnO and SnO_2 based devices, respectively. Electroimpedance and electrical measurements show that the light stability improvement can be attributed to the lower defect formation at the active layer interface with the metal oxide for the 10:90 ratio ZnO:SnO_2 ETL compared to the pristine ZnO, SnO_2, or other ratios of ZnO:SnO_2 ETL.

MATERIALS AND METHODS

Materials. Prepatterned glass-ITO substrates T1 (PBDB-TF-T1) and IT-4F were purchased from Ossila Ltd. The stannic oxide (SnO_2 N-31) and zinc oxide (ZnO N-10-Flex) in a mixture of butanols (2.5 wt %) were supplied by Avantama AG. Silver (Ag) pellets (99.99%) were purchased from Kurt J. Lesker Company. All of the other chemicals in this study were purchased from Sigma-Aldrich.

Device Fabrication. The ITO/glass substrates were sequentially sonicated in acetone and 2-propanol for 10 min and dried with N_2 before use. The mixed metal oxides and the pristine ZnO and SnO_2 metal oxide nanoparticle inks were blade coated at 70 °C on top of on ITO/glass substrates in air without any further treatment, resulting in ∼30 nm thick ETLs. The active layer solution T1:IT4F (1:1.2 wt %) dissolved in *o*-xylene were blade coated at 70 °C on top of the various underlayers in air and annealed at 100 °C for 10 min in a glovebox. *o*-Xylene was selected as a less toxic organic solvent compared to commonly used halogenated solvents (e.g., chlorobenzene), rendering the process more compatible for industrial large-scale fabrication. To complete the devices 10 nm MoO_3 and 100 nm Ag were thermally evaporated resulting in a 4 mm^2 active area.

Characterization. The thickness of the films was measured with a Veeco Dektak 150 profilometer. AFM images were obtained using a Nanosurf easy scan 2 controller in tapping mode. For the current−voltage (J−V) characterization a 1 sun calibrated (100 mW/cm^2, Oriel 91150 V calibration cell) Newport Solar simulator equipped with a Xe lamp was used. The J−V curves were obtained by using an Ossila Solar Cell I-V Test System. To extract the series resistance (R_s) and shunt resistance (R_{sh}) the slope of the light J−V curve was calculated at the region close to the V_{oc} and J_s, respectively. The light stability of the unencapsulated devices was determined following ISOS-L2, where according to the protocol the measuring conditions are light source from solar simulator, device temperature 65 or 85 °C,

https://doi.org/10.1021/acsaelm.5c00201
ACS Appl. Electron. Mater. 2025, 7, 3940−3946

ambient environment, and load at MPP or open circuit (V_{oc}).[27] In our case, the unencapsulated devices were exposed to 100 mW/cm^2 solar simulated light in an ambient environment (RH ≈ 50%, temp ≈ 23 °C) while the devices were heated at ∼65 °C during the measurement. Each device was $J-V$ scanned between −0.5 and 1.2 V every 2 min, and between it was kept at open circuit conditions. The extraction of the total energy produced by each sample was calculated by intergrating the power obtained by each sequential measurement until it reached 80% of the initial PCE. The absorption measurements were performed with a Shimadzu UV-2700 UV−vis optical spectrophotometer. Electroimpedance spectroscopy (EIS) measurements were obtained using a Metrohm Autolab PGSTAT 302N. Mott−Schottky measurement was obtained by applying a small AC perturbation of 10 mV, a frequency of 1000 Hz, and dark conditions. $-Z''$-Frequency measurement was obtained by applying a small AC perturbation of 10 mV at 0.9 V bias and under dark conditions.

RESULTS AND DISCUSSION

Inverted OSCs with the structure ITO/ZnO:SnO_2 mixture ETL/PBDB-TF-T1 (T1):IT4F/MoO_3/Ag were fabricated applying a full range of ZnO:SnO_2 ratios as ETLs. Specifically, for the preparation of the various mixed ETLs, ZnO and SnO_2 metal oxide nanoparticle inks were mixed in volume ratios 10:90, 30:70, 50:50, 70:30, and 90:10. Each batch of inverted OSCs incorporating mixed metal oxide or pristine metal oxide ETLs consists of 16 different devices.

Figure S1 depicts the $J-V$ curves of the best obtained PCE for each device structure while the corresponding PV parameters as well as the mean PV parameters with the standard deviation in parentheses are shown in Table 1 (Figure S2a−d as graph). It is seen that increasing the ZnO ratio in the mixed metal oxide ETL leads to a higher mean PCE, with the highest mean PCE (10.73%) obtained for pristine ZnO ETL. Regarding the PV parameters, ratios of ZnO above 50% increases the mean V_{oc} from 0.94 to 0.96 V. The mean J_{sc} and FF also show an increasing trend for higher ratios of ZnO within the ETL. The lower PCE of the SnO_2 compared to ZnO based devices is ascribed to the higher energy offset of the LUMO energy levels between the IT4F (−4.10 eV)/SnO_2 (−4.5 eV) compared to IT4F (−4.10)/ZnO (−4.3 eV) (literature reported values) resulting in V_{oc} losses.[28−30] Additionally, the higher mean series resistances (R_s) (Figure S2e) and the lower shunt resistance (R_{sh}) (Figure S2f) result in lower FF and J_{sc}.

The unencapsulated devices were tested under the ISOS-L2 protocol to examine the stability of the devices. Figure 1a−d shows the normalized PCE, J_{sc}, V_{oc}, and FF with respect to light exposure time for the devices incorporating various ratios of mixed ZnO:SnO_2 ETLs. The ZnO:SnO_2 10:90 mixture demonstrated the highest stability, prolonging the lifetime (80% of the initial PCE, T_{80}) by ∼16.5 times compared to ZnO and by ∼2.8 times compared to SnO_2. Specifically, the pristine SnO_2 based devices reached $T80$ within ∼100 min after a light soaking increase of the initial PCE ascribed to photoinduced passivation of the surface defects.[31] The devices based on ZnO:SnO_2 ratios 10:90, 30:70, and 50:50 reached T_{80} after ∼280, ∼150, and ∼80 min, respectively. On the other hand, when the ZnO content within the ETL was above 50% T_{80} was reached after only 17−30 min. To estimate the trade-off between initial PCE and lifetime, we calculated the produced energy until T_{80} (Table 2). The highest electrical energy (1434 μWh/cm^2) was provided by the OSC incorporating the ZnO:SnO_2 ratio 10:90 ETL. The produced energy is about ∼13.2 and ∼3.0 times higher compared to the corresponding ZnO and SnO_2 based OSCs. Thus, the lower PCE of the 10:90 ZnO:SnO_2 based device compared to devices with higher ratios of ZnO content is compensated by the improved lifetime, resulting in more efficient devices. Figure S3 shows the T_{80} lifetime (left axis) and the corresponding calculated produced energy (right axis) for the OSC based on the various ratios of ZnO:SnO_2 ETL, visualizing the strong correlation between these two parameters.

Table 2. Electrical Energy Produced under ISOS-L2 Protocol until T_{80} by the Unencapsulated T1:IT4F Based Inverted OSC Incorporating Various Ratios of Mixed ZnO:SnO_2 ETL

ZnO:SnO_2 (%V)	E (μWh/cm^2)
0:100	480
10:90	1434
30:70	908
50:50	442
70:30	181
90:10	156
100:0	109

Further investigation was conducted for a deeper understanding of the lifetime enhancement of the OSC incorporating ZnO:SnO_2 10:90. The surface topography of the various films fabricated on top of indium tin oxide (ITO) substrates was obtained using AFM. Figure S4a,g presents the obtained topography images (10 μm × 10 μm) of the various metal oxide films applying the same processing parameters used for the fabrication of the corresponding OSC. The extracted roughness (RMS) of the films demonstrates negligible difference between the various films ranging from 3.7 to 4.6 nm. From the corresponding AFM phase images (Figure S5a−g) we can infer that all the films under study exhibit pinhole-free films based on the observation of the smooth frequency images. Thus, we rule out that such small morphological differences of the ETL films affect the lifetime performances of the OSC under study.

Figure 2a shows the UV−vis absorption graph of various mixed metal oxide ZnO:SnO_2 ETLs fabricated on top of the glass substrates. The films exhibit an increasing absorption coefficient at wavelengths shorter than 400 nm for higher ratios of ZnO within the ZnO:SnO_2 ETL. Thus, illumination with UV containing light will result in a higher number of photogenerated electron−hole pairs in the metal oxide ETL, which in turn increases the photoreactivity of the layers. On the other hand, SnO_2 has a higher band gap and thus lower absorption coefficient at the near UV region resulting in lower electron−hole pair photogeneration, rendering the SnO_2 less photoreactive. However, a marginal degradation of the interface results in the formation of energetic barriers and trap states that impedes the efficient charge transfer to the contacts.[32] Thus, and given the light stability measurement shown above, pristine SnO_2 can degrade the very delicate metal oxide/active layer interface. The addition of 10% ZnO NP in SnO_2 marginally affects the absorption at wavelengths shorter than 400 nm. Thus, we rule out that the difference in lifetime between pristine and 10% ZnO based devices is affected by UV absorption properties.

Figure 2b−d and Figure S6a−d present the Mott−Schottky plots of unencapsulated T1:IT4F based inverted OSCs incorporating the various ratios of mixed metal oxide

https://doi.org/10.1021/acsaelm.5c00201
ACS Appl. Electron. Mater. 2025, 7, 3940−3946

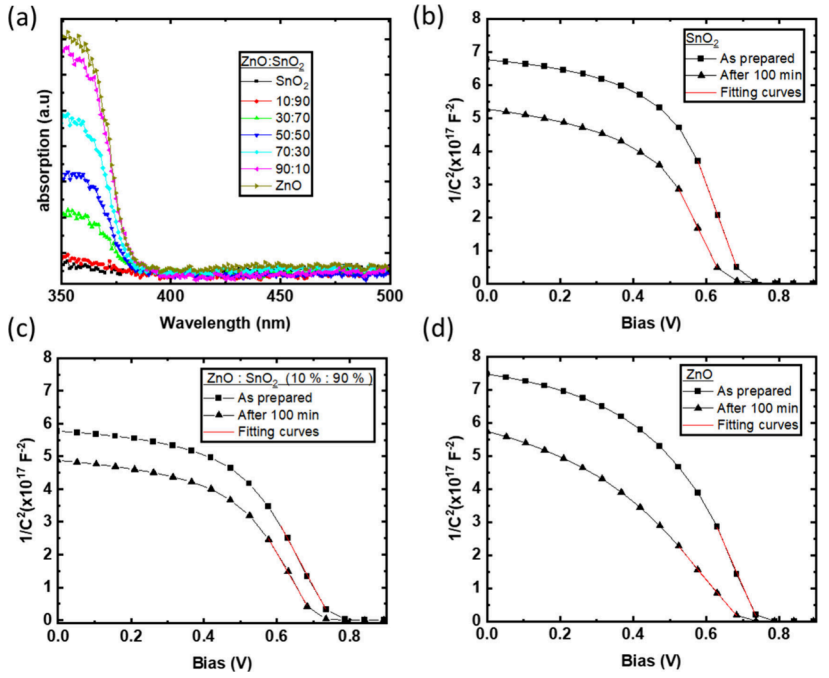

Figure 2. (a) UV−vis absorption graph of mixed oxide ZnO:SnO_2 ETL and Mott−Schottky plots of unencapsulated T1:IT4F based inverted OSCs incorporating (b) SnO_2, (c) mixed oxide ZnO:SnO_2 10:90 ETL, and (d) ZnO for the as-prepared devices and after 100 min under the ISOS-L2 protocol.

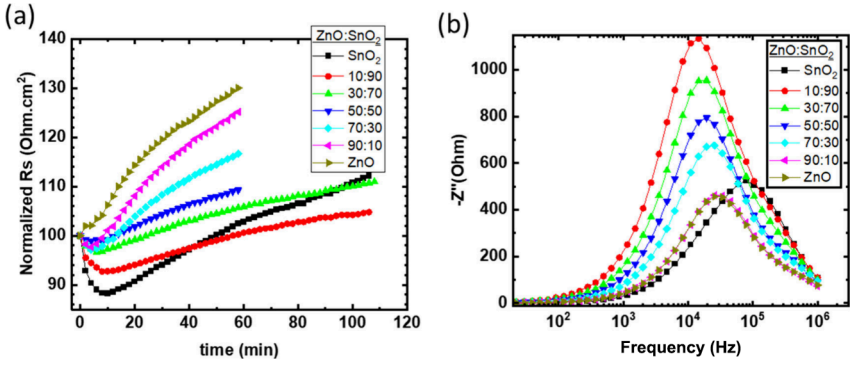

Figure 3. (a) Normalized series resistance of unencapsulated T1:IT4F based inverted OSCs incorporating various ratios of mixed oxide ZnO:SnO_2 ETL under ISOS-L2 and (b) the $-Z''$−frequency of the as-preparaed device.

ZnO:SnO_2 ETLs on the as-prepared unencapsulated inverted OSC and after 100 min under the ISOS-L2 protocol. Mott−Schottky plots can provide information about the doping profile of the semiconductor through the modulation of the depletion zone according to the relation

$$\frac{1}{C^2} = \frac{2(V_{bi} - V)}{A^2 e \varepsilon \varepsilon_0 N}$$

where N is the doping density.[33,34] Thus, we can get an estimation for the light induced formation of a defect state that can act as dopants close to the interface by calculating the slope in the Mott−Schottky plot at bias close to V_{bi} before and after degradation. The increases in slope (order of magnitude 10^{17}) before and after the illumination are 0.77 and 1.27 for the SnO_2 and ZnO ETL based inverted OSC, respectively. In contrast, the ZnO:SnO_2 10:90 ETL based device exhibits the lowest slope increase by only 0.13, pointing to lower ETL induced defect formation close to the interface. The calculated slopes for the 30:70, 50:50, 70:30, and 90:10 ETL based devices increase by 0.49, 0.55, 1.30, and 1.29, respectively.

We also calculated the relative change of R_s from the light J−V curves with respect to the time (Figure 3a). The R_s increase can be ascribed to the increase of the electron extraction barrier (higher contact resistance) due to the widening of energetic mismatch of the metal oxide/IT4F interface and the reduced electron mobility induced by the formed defects.[32] The ZnO:SnO_2 10:90 ETL based inverted OSC shows the lowest R_s after 100 min illumination compared to any other ratio of ZnO:SnO_2 in accordance with the Mott−Schottky results. Impedance ($-Z''$)−frequency measurements were performed to gain a better insight into the function of the ZnO:SnO_2 10:90 based inverted OSCs. Figure 3b) shows the $-Z''$−frequency spectra of the as-prepared devices. Each peak represents a characteristic relaxation process, where the peak frequency (f_p) corresponds to the relaxation time (τ) of the process through the inverse relationship $\tau = f^{-1}/2\pi$. The ZnO or SnO_2 based inverted OSCs exhibit a characteristic f_p for each device. The inverted OSC incorporating ZnO:SnO_2

https://doi.org/10.1021/acsaelm.5c00201
ACS Appl. Electron. Mater. 2025, 7, 3940−3946

10:90 clearly shows an overlap of at least two peak frequencies that can be reproduced by the SnO_2 based device f_p and a new peak f_p with 1 order of magnitude lower frequency. Thus, an additional relaxation process is present with 1 order of magnitude higher τ. Considering that the content of ZnO nanoparticles in the ZnO:SnO_2 10:90 based ETL is quite low, the vast majority of ZnO nanoparticles are dispersed within the SnO_2 nanoparticle matrix, and thus a negligible number of ZnO NPs are in physical contact with the active layer. Thus, we exclude that this new peak originates from a detectable charge transfer process at the ZnO:SnO_2 (10:90)/active layer interface between the ZnO NPs and the active layer but rather signifies a charge transfer process at the SnO_2/ZnO heterojunction. Based on the above, we argue that under working conditions and due to the ZnO/SnO_2 heterojunction the UV light photogenerated holes in SnO_2 are transferred to the ZnO HOMO (lower HOMO level of SnO_2 compared to ZnO). The holes, which would otherwise be transferred to the metal-oxide/active layer interface are now trapped in ZnO nanoparticles due to the potential well. When a higher concentration of ZnO nanoparticles is present in the ZnO/SnO_2 ETL, the higher surface area of the ZnO NPs results in physical contact between the ZnO NPs and the active layer, promoting the hole charges to the metal oxide/active layer interface. The trapped holes (minority carriers) will be annihilated by the electrons (majority carriers) through recombination, inducing a reduction of the R_{sh}. This argument is in accordance with the findings presented in Figure S2f, where for ZnO:SnO_2 10:90 the devices exhibit the lowest mean R_{sh} due to the highest number of trapped holes, as discussed above. On the other hand, the photogenerated valence electrons in SnO_2 experience an energetic barrier that blocks their easy transfer from SnO_2 to ZnO, while the photogenerated electrons in ZnO easily drift to SnO_2 due to lower LUMO levels of SnO_2 (higher electron affinity).

A suggested degradation mechanism is attributed to the photogenerated electron hole pair in the metal oxide that consists of reductive and oxidative species, respectively. These photogenerated charges in the metal oxide ETL can oxidize or reduce directly or indirectly the organic molecules of the active layer at the interface, resulting in device performance degradation.[28,35,36] Under working conditions, most of the electron charges drift and are collected by the metal contact, while the generated holes close to the interface with the active layer can drift/diffuse to the metal oxide/active layer interface. These holes can oxidize the surface absorbed water or hydroxyl groups, producing hydroxyl radicals ($^{\bullet}OH$).[37] The reactivity of the metal oxide occurs predominantly on the surface of the ETL, resulting in the oxidation of the active layer inducing impurities near the surface of the active layer.[38] The addition of a low density of ZnO NPs within the SnO_2 nanoparticle ETL result in the dispersion of the ZnO NPs in the bulk SnO_2. This composite structure drifts and traps the generated holes in the potential well formed by the SnO_2/ZnO contact, as shown by the $-Z''-$frequency measurements, restraining the number of holes that can reach the ETL surface. Thus, the defect formation is reduced at the metal oxide/active layer interface, which agrees with the Mott−Schottky data and lower increase of the device R_s as a function of exposure time. A schematic illustration of the above-described process is presented in Figure S7.

Thus, we propose that the dispersion of 10% ZnO nanoparticles within the SnO_2 nanoparticles can act as hole scavengers that reduce the photocatalytic reaction of the metal oxide based ETL surface leading to improved stability of the OSC under the ISOS-L2 protocol.

CONCLUSION

In conclusion, we demonstrate the fabrication of inverted OSCs based on the binary active layer system PBDB-TF-T1 (T1):IT4F using a full range of ZnO:SnO_2 NP mixtures as ETLs. Unencapsulated solar cell devices incorporating 10:90 ZnO:SnO_2, even though they provided a lower PCE, the total produced power until reaching 80% of the initial efficiency is about ∼13.2 and ∼3.0 times higher compared to the corresponding ZnO and SnO_2 based inverted OSCs. This results from improved stability (ISOS-L2 protocol) that prolongs lifetime (80% of the initial PCE, T_{80}) by ∼16.5 times compared to ZnO and by ∼2.8 times compared to SnO_2.The lifetime improvement for 10:90 ZnO:SnO_2 is attributed to lower impurity formation at the active layer interface with the metal oxide. Specifically, we propose that the dispersion of 10% ZnO NPs within the SnO_2 NPs acts as photogenerated hole scavengers, resulting in a reduced photocatalytic reactivity that mitigates active layer interface degradation.

ASSOCIATED CONTENT

Supporting Information

The Supporting Information is available free of charge at https://pubs.acs.org/doi/10.1021/acsaelm.5c00201.

J−*V* curves of the highest PCE devices under 1 sun simulated light (AM 1.5) of the unencapsulated inverted T1:IT4F based OSCs incorporating various ratios of mixed oxide ZnO:SnO_2 ETLs, mean PCE, J_{sc}, V_{oc}, FF, R_s, and R_{sh} under the ISOS-L2 protocol of the unencapsulated inverted T1:IT4F based OSCs incorporating various ratios of mixed oxide ZnO:SnO_2 ETLs, T_{80} lifetimes (left axis) and the corresponding calculated produced energies (right axis) of the unencapsulated T1:IT4F based inverted OSCs incorporating various ratios of mixed oxide ZnO:SnO_2 ETLs, AFM topography images (10 × 10 μm) of SnO_2, 10:90, 30:70, 50:50, 70:30, and 90:10 ZnO/SnO_2, and ZnO ETLs fabricated on top of ITO, AFM phase images (10 × 10 μm) of SnO_2, 10:90, 30:70, 50:50, 70:30, and 90:10 ZnO:SnO_2, and ZnO ETLs fabricated on top of ITO, Mott−Schottky plots of unencapsulated T1:IT4F based inverted OSCs incorporating mixed metal oxide ZnO:SnO_2 30:70, 50:50, 70:30, and 90:10 ETLs for the as-prepared and after 100 min ISOS-L2 protocol, and schematic illustration of the restrained photooxidation at the mixed metal oxide/active layer interface due to the presence of a low density of ZnO nanoparticles within the SnO_2 ETL (PDF)

AUTHOR INFORMATION

Corresponding Authors

Apostolos Ioakeimidis − *Molecular Electronics and Photonics Research Unit, Department of Mechanical Engineering and Materials Science and Engineering, Cyprus University of Technology, Limassol 3603, Cyprus;* orcid.org/0000-0003-3974-6574; Email: a.ioakeimidis@cut.ac.cy

Stelios A. Choulis − *Molecular Electronics and Photonics Research Unit, Department of Mechanical Engineering and*

https://doi.org/10.1021/acsaelm.5c00201
ACS Appl. Electron. Mater. 2025, 7, 3940−3946

Materials Science and Engineering, Cyprus University of Technology, Limassol 3603, Cyprus; orcid.org/0000-0002-7899-6296; Email: stelios.choulis@cut.ac.cy

Authors

Fedros Galatopoulos − *Molecular Electronics and Photonics Research Unit, Department of Mechanical Engineering and Materials Science and Engineering, Cyprus University of Technology, Limassol 3603, Cyprus*

Alina Hauser − *Avantama AG, Staefa 8712, Switzerland*

Michael Rossier − *Avantama AG, Staefa 8712, Switzerland*

Complete contact information is available at: https://pubs.acs.org/10.1021/acsaelm.5c00201

Funding

This project has received funding from the European Union's Horizon 2020 research and innovation program under grant agreement No 862474 (project RoLA-FLEX).

Notes

The authors declare no competing financial interest.

REFERENCES

(1) Zhu, L.; Zhang, M.; Xu, J.; Li, C.; Yan, J.; Zhou, G.; Zhong, W.; Hao, T.; Song, J.; Xue, X.; Zhou, Z.; Zeng, R.; Zhu, H.; Chen, C. C.; MacKenzie, R. C. I.; Zou, Y.; Nelson, J.; Zhang, Y.; Sun, Y.; Liu, F. Single-Junction Organic Solar Cells with over 19% Efficiency Enabled by a Refined Double-Fibril Network Morphology. *Nat. Mater.* **2022**, *21* (6), 656−663.

(2) Li, S.; He, C.; Chen, T.; Zheng, J.; Sun, R.; Fang, J.; Chen, Y.; Pan, Y.; Yan, K.; Li, C.-Z.; Shi, M.; Zuo, L.; Ma, C.-Q.; Min, J.; Liu, Y.; Chen, H. Refined Molecular Microstructure and Optimized Carrier Management of Multicomponent Organic Photovoltaics toward 19.3% Certified Efficiency. *Energy Environ. Sci.* **2023**, *16* (5), 2262−2273.

(3) Ding, P.; Yang, D.; Yang, S.; Ge, Z. Stability of Organic Solar Cells: Toward Commercial Applications. *Chem. Soc. Rev.* **2024**, *53* (5), 2350−2387.

(4) Rafique, S.; Abdullah, S. M.; Sulaiman, K.; Iwamoto, M. Fundamentals of Bulk Heterojunction Organic Solar Cells: An Overview of Stability/Degradation Issues and Strategies for Improvement. *Renew. Sustain. Energy Rev.* **2018**, *84*, 43−53.

(5) Lu, Q.; Yang, Z.; Meng, X.; Yue, Y.; Ahmad, M. A.; Zhang, W.; Zhang, S.; Zhang, Y.; Liu, Z.; Chen, W. A Review on Encapsulation Technology from Organic Light Emitting Diodes to Organic and Perovskite Solar Cells. *Adv. Funct. Mater.* **2021**, *31* (23), 2100151.

(6) Duan, L.; Uddin, A. Progress in Stability of Organic Solar Cells. *Adv. Sci.* **2020**, *7* (11), No. 1903259.

(7) Burlingame, Q.; Huang, X.; Liu, X.; Jeong, C.; Coburn, C.; Forrest, S. R. Intrinsically Stable Organic Solar Cells under High-Intensity Illumination. *Nature* **2019**, *573* (7774), 394−397.

(8) Li, Y.; Huang, B.; Zhang, X.; Ding, J.; Zhang, Y.; Xiao, L.; Wang, B.; Cheng, Q.; Huang, G.; Zhang, H.; Yang, Y.; Qi, X.; Zheng, Q.; Zhang, Y.; Qiu, X.; Liang, M.; Zhou, H. Lifetime over 10000 h for Organic Solar Cells with Ir/IrOx Electron-Transporting Layer. *Nat. Commun.* **2023**, *14* (1), 1241.

(9) Liu, Y.; Liu, B.; Ma, C.; Huang, F.; Feng, G.; Chen, H.; Hou, J.; Yan, L.; Wei, Q.; Luo, Q.; Bao, Q.; Ma, W.; Liu, W.; Li, W.; Wan, X.; Hu, X.; Han, Y.; Li, Y.; Zhou, Y.; Zou, Y.; Chen, Y.; Li, Y.; Chen, Y.; Tang, Z.; Hu, Z.; Zhang, Z.-G.; Bo, Z. Recent Progress in Organic Solar Cells (Part I Material Science). *Sci. China Chem.* **2022**, *65* (2), 224−268.

(10) Liu, Y.; Liu, B.; Ma, C.-Q.; Huang, F.; Feng, G.; Chen, H.; Hou, J.; Yan, L.; Wei, Q.; Luo, Q.; Bao, Q.; Ma, W.; Liu, W.; Li, W.; Wan, X.; Hu, X.; Han, Y.; Li, Y.; Zhou, Y.; Zou, Y.; Chen, Y.; Liu, Y.; Meng, L.; Li, Y.; Chen, Y.; Tang, Z.; Hu, Z.; Zhang, Z.-G.; Bo, Z. Recent Progress in Organic Solar Cells (Part II Device Engineering). *Sci. China Chem.* **2022**, *65* (8), 1457−1497.

(11) Xue, R.; Zhang, J.; Li, Y.; Li, Y. Organic Solar Cell Materials toward Commercialization. *Small* **2018**, *14* (41), 1801793.

(12) Qiu, L.; Ono, L. K.; Qi, Y. Advances and Challenges to the Commercialization of Organic−Inorganic Halide Perovskite Solar Cell Technology. *Mater. Today Energy* **2018**, *7*, 169−189.

(13) Wadsworth, A.; Moser, M.; Marks, A.; Little, M. S.; Gasparini, N.; Brabec, C. J.; Baran, D.; McCulloch, I. Critical Review of the Molecular Design Progress in Non-Fullerene Electron Acceptors towards Commercially Viable Organic Solar Cells. *Chem. Soc. Rev.* **2019**, *48* (6), 1596−1625.

(14) Yang, W.; Wang, W.; Wang, Y.; Sun, R.; Guo, J.; Li, H.; Shi, M.; Guo, J.; Wu, Y.; Wang, T.; Lu, G.; Brabec, C. J.; Li, Y.; Min, J. Balancing the Efficiency, Stability, and Cost Potential for Organic Solar Cells via a New Figure of Merit. *Joule* **2021**, *5* (5), 1209−1230.

(15) Sorrentino, R.; Kozma, E.; Luzzati, S.; Po, R. Interlayers for Non-Fullerene Based Polymer Solar Cells: Distinctive Features and Challenges. *Energy Environ. Sci.* **2021**, *14* (1), 180−223.

(16) Ioakeimidis, A.; Hauser, A.; Rossier, M.; Linardi, F.; Choulis, S. A. High-Performance Non-Fullerene Acceptor Inverted Organic Photovoltaics Incorporating Solution Processed Doped Metal Oxide Hole Selective Contact. *Appl. Phys. Lett.* **2022**, *120* (23), 233301.

(17) Yu, Z.; Liu, W.; Fu, W.; Zhang, Z.; Yang, W.; Wang, S.; Li, H.; Xu, M.; Chen, H. An Aqueous Solution-Processed CuOX Film as an Anode Buffer Layer for Efficient and Stable Organic Solar Cells. *J. Mater. Chem. A* **2016**, *4* (14), 5130−5136.

(18) Fu, P.; Yao, T.; Wang, P.; Yang, Q.; Ni, Y.; Guo, X.; Li, C. Efficient Non-Fullerene Organic Solar Cells with Low-Temperature Solution-Processing Ferrous Oxides as Hole Transport Layer. *Org. Electron.* **2021**, *93*, No. 106139.

(19) Ahmad, N.; Zhou, H.; Fan, P.; Liang, G. Recent Progress in Cathode Interlayer Materials for Non-fullerene Organic Solar Cells. *EcoMat* **2022**, *4* (1), 1−33.

(20) Li, S.; Fu, Q.; Meng, L.; Wan, X.; Ding, L.; Lu, G.; Lu, G.; Yao, Z.; Li, C.; Chen, Y. Achieving over 18% Efficiency Organic Solar Cell Enabled by a ZnO-Based Hybrid Electron Transport Layer with an Operational Lifetime up to 5 Years. *Angew. Chemie - Int. Ed.* **2022**, *61*, 100190.

(21) Garcia Romero, D.; Di Mario, L.; Yan, F.; Ibarra-Barreno, C. M.; Mutalik, S.; Protesescu, L.; Rudolf, P.; Loi, M. A. Understanding the Surface Chemistry of SnO 2 Nanoparticles for High Performance and Stable Organic Solar Cells. *Adv. Funct. Mater.* **2024**, *34* (6), 1−9.

(22) Hu, L.; Jiang, Y.; Sun, L.; Xie, C.; Qin, F.; Wang, W.; Zhou, Y. Significant Enhancement of Illumination Stability of Nonfullerene Organic Solar Cells via an Aqueous Polyethylenimine Modification. *J. Phys. Chem. Lett.* **2021**, *12* (10), 2607−2614.

(23) Xu, X.; Xiao, J.; Zhang, G.; Wei, L.; Jiao, X.; Yip, H. L.; Cao, Y. Interface-Enhanced Organic Solar Cells with Extrapolated T80 Lifetimes of over 20 years. *Sci. Bull.* **2020**, *65* (3), 208−216.

(24) Hadmojo, W. T.; Isikgor, F. H.; Lin, Y.; Ling, Z.; He, Q.; Faber, H.; Yengel, E.; Ali, R.; Samad, A.; Ardhi, R. E. A.; Jeong, S. Y.; Woo, H. Y.; Schwingenschlögl, U.; Heeney, M.; Anthopoulos, T. D. Stable Organic Solar Cells Enabled by Simultaneous Hole and Electron Interlayer Engineering. *ENERGY Environ. Mater.* **2024**, *7*, 1−8.

(25) Jiang, Y.; Sun, L.; Jiang, F.; Xie, C.; Hu, L.; Dong, X.; Qin, F.; Liu, T.; Hu, L.; Jiang, X.; Zhou, Y. Photocatalytic Effect of ZnO on the Stability of Nonfullerene Acceptors and Its Mitigation by SnO 2 for Nonfullerene Organic Solar Cells. *Mater. Horizons* **2019**, *6* (7), 1438−1443.

(26) Park, K.; Kim, J.-H.; Jin, J. S.; Moon, H.; Oh, J.; Lee, S.; Ki, T.; Jeong, H.-S.; Jeong, S.; Jang, S.-Y.; Kang, H.; Lee, K. Overcoming the Interfacial Photocatalytic Degradation of Nonfullerene Acceptor-Based Organic Photovoltaics by Introducing a UV-A-Insensitive Titanium Suboxide Layer. *ACS Appl. Mater. Interfaces* **2024**, *16* (3), 3778−3785.

(27) Reese, M. O.; Gevorgyan, S. A.; Jorgensen, M.; Bundgaard, E.; Kurtz, S. R.; Ginley, D. S.; Olson, D. C.; Lloyd, M. T.; Morvillo, P.; Katz, E. A.; Elschner, A.; Haillant, O.; Currier, T. R.; Shrotriya, V.; Hermenau, M.; Riede, M.; Kirov, K. R.; Trimmel, G.; Rath, T.; Inganäs, O.; Zhang, F.; Andersson, M.; Tvingstedt, K.; Lira-Cantu,

M.; Laird, D.; McGuiness, C.; Gowrisanker, S.; Pannone, M.; Xiao, M.; Hauch, J.; Steim, R.; Delongchamp, D. M.; Rösch, R.; Hoppe, H.; Espinosa, N.; Urbina, A.; Yaman-Uzunoglu, G.; Bonekamp, J. B.; Van Breemen, A. J. J. M.; Girotto, C.; Voroshazi, E.; Krebs, F. C. Consensus Stability Testing Protocols for Organic Photovoltaic Materials and Devices. *Sol. Energy Mater. Sol. Cells* **2011**, *95* (5), 1253−1267.

(28) Bhattacharjee, A.; Ahmaruzzaman, M.; Sinha, T. A Novel Approach for the Synthesis of SnO2 Nanoparticles and Its Application as a Catalyst in the Reduction and Photodegradation of Organic Compounds. *Spectrochim. Acta Part A Mol. Biomol. Spectrosc.* **2015**, *136* (PB), 751−760.

(29) Yu, J. H.; Heo, S. B.; Shin, J. S.; Kang, S. J. Improvement of the Electron Transport Behavior in Quantum-Dot Light-Emitting Diodes Using a Low-Temperature Processable ZnO. *Curr. Appl. Phys.* **2020**, *20* (2), 366−370.

(30) Xiong, L.; Guo, Y.; Wen, J.; Liu, H.; Yang, G.; Qin, P.; Fang, G. Review on the Application of SnO 2 in Perovskite Solar Cells. *Adv. Funct. Mater.* **2018**, *28* (35), 1−18.

(31) Suo, Z.; Xiao, Z.; Li, S.; Liu, J.; Xin, Y.; Meng, L.; Liang, H.; Kan, B.; Yao, Z.; Li, C.; Wan, X.; Chen, Y. Efficient and Stable Inverted Structure Organic Solar Cells Utilizing Surface-Modified SnO2 as the Electron Transport Layer. *Nano Energy* **2023**, *118* (PB), No. 109032.

(32) Fraga Domínguez, I.; Distler, A.; Lüer, L. Stability of Organic Solar Cells: The Influence of Nanostructured Carbon Materials. *Adv. Energy Mater.* **2017**, *7* (10), 1601320.

(33) Tokmoldin, N.; Hosseini, S. M.; Raoufi, M.; Phuong, L. Q.; Sandberg, O. J.; Guan, H.; Zou, Y.; Neher, D.; Shoaee, S. Extraordinarily Long Diffusion Length in PM6:Y6 Organic Solar Cells. *J. Mater. Chem. A* **2020**, *8* (16), 7854−7860.

(34) Pang, H. S.; Xu, H.; Tang, C.; Meng, L. K.; Ding, Y.; Xiao, J.; Liu, R. L.; Pang, Z. Q.; Huang, W. Capacitance Methodology for Investigating Defect States in Energy Gap of Organic Semiconductor. *Org. Electron.* **2019**, *65*, 275−299.

(35) Liao, Q.; Kang, Q.; Yang, Y.; Zheng, Z.; Qin, J.; Xu, B.; Hou, J. Highly Stable Organic Solar Cells Based on an Ultraviolet-Resistant Cathode Interfacial Layer. *CCS Chem.* **2022**, *4* (3), 938−948.

(36) Jiang, P.; Hu, L.; Sun, L.; Li, Z.; Han, H.; Zhou, Y. On the Interface Reactions and Stability of Nonfullerene Organic Solar Cells. *Chem. Sci.* **2022**, *13* (17), 4714−4739.

(37) Uddin, M. T.; Hoque, M. E.; Chandra Bhoumick, M. Facile One-Pot Synthesis of Heterostructure SnO 2 /ZnO Photocatalyst for Enhanced Photocatalytic Degradation of Organic Dye. *RSC Adv.* **2020**, *10* (40), 23554−23565.

(38) Park, S.; Son, H. J. Intrinsic Photo-Degradation and Mechanism of Polymer Solar Cells: The Crucial Role of Non-Fullerene Acceptors. *J. Mater. Chem. A* **2019**, *7* (45), 25830−25837.

https://doi.org/10.1021/acsaelm.5c00201
ACS Appl. Electron. Mater. 2025, 7, 3940−3946